

Void space and scaffold analysis of packed particles: applications in granular biomaterials

Lindsay Riley

Duke University

Peter Cheng

Ninjabyte Computing

Tatiana Segura (✉ tatiana.segura@duke.edu)

Duke University <https://orcid.org/0000-0003-1569-8686>

Article

Keywords:

Posted Date: August 11th, 2022

DOI: <https://doi.org/10.21203/rs.3.rs-1766378/v1>

License: © ⓘ This work is licensed under a Creative Commons Attribution 4.0 International License.

[Read Full License](#)

Void space and scaffold analysis of packed particles: applications in granular biomaterials

Lindsay Riley¹, Peter Cheng², Tatiana Segura^{1,3*}

¹Department of Biomedical Engineering, Duke University

²Ninjabyte Computing

³Department of Medicine, Neurology, Dermatology, Duke University

* To whom correspondence should be addressed

Tatiana Segura

tatiana.segura@duke.edu

Abstract

We have developed a tool for analyzing packed particles in response to the growing popularity of granular biomaterials. Granular hydrogels, including microporous annealed particle (MAP) scaffolds, are a class of material used for therapeutic applications due to their unique properties, including micro-porosity between particles. The microarchitecture of granular materials is challenging to study, which leads many in the field to report the unreliable metric of void volume fraction and/or 2D-slice approximations to 'pore size' as the only characterizations of void space. In response, we have created LOVAMAP, a custom software that combines techniques from computational geometry and graph theory to segment the void space into 3-D pores, which are the natural pockets of open space. LOVAMAP's 44 scaffold features provide the user with a quantitative profile that describes both the interior and entrances of the scaffold. Our visually-rich outputs address topics like void space size, shape, connectivity, paths, isotropy/anisotropy, ligand availability, and infiltration/migration restrictions. Using LOVAMAP, we have studied 60 different types of granular scaffolds, including real MAP scaffolds with corresponding cell data. We use higher dimensional analysis to show that output data from our software can be used to classify types of 3-D pores, as well as characterize entire scaffolds by generating a numeric 'fingerprint.' In conjunction with cell data, LOVAMAP reveals relationships between neurosphere formation and scaffold void space geometry. LOVAMAP is an enabling technology with broad applications for granular biomaterial research and for all fields that study granular material.

Background

Packed particles and the void space (interstitial space, pore space) surrounding them are a trending research topic because of the increasing popularity of granular biomaterials. Granular materials are appealing for a number of applications, including injectable tissue mimics and 3-D bioprinting, because they offer unique properties like shear-thinning behavior, increased material surface area, and the option for discrete heterogeneity^{1, 2}. Granular materials made from hydrogel microparticles (microgels) have been used to promote wound healing in a number of disease models, including stroke³, myocardial infarction⁴, cutaneous wounds⁵, and spinal cord injury⁶. When microgels pack together, they form a 3-D structure referred to as a granular scaffold, and when the microgels of a granular scaffold are linked together, the resulting stable structure is termed a microporous annealed particle (MAP) scaffold⁷. Packed microgels form void space micro-porosity throughout the scaffold, which allows for unhindered cell infiltration and migration between the particles. Many studies support the notion that local geometry influences cell behavior⁸⁻¹³, and in granular scaffolds, the local geometry sensed by cells is the microarchitecture of the void space. Therefore, we aim to understand the internal geometry of granular scaffolds to improve material design.

In the biomaterials field, porosity that is approximated using 2-D microscope images is the most commonly-reported quantification of scaffold void space. Porosity is typically reported as a void volume fraction or as a distribution of 2-D 'pore' length measurements. We have previously revealed the nuances of reporting such approximations to porosity¹⁴, and we make the argument that void volume fraction and 2-D approximations of pores are inadequate as standalone metrics because they disregard the complexity and geometrical variety found in local pockets of 3-D void space.

Packed particles have been studied extensively in other fields (mathematics, physics, geoscience, chemistry, agriculture, etc.) without consideration for how void space geometry influences the behavior of cells. Research commonly focuses on the particles themselves, where methods have been developed to identify particle boundaries¹⁵⁻¹⁷ or construct the graph of touching particles to study particle connectivity, packing configuration, and stress force chains¹⁸⁻²³. However, these results fail to characterize void space. Some particle-focused research has included information about void space,

such as Delaunay tessellation by particle centroids to identify the smallest void subunits formed by tetrahedral particle stacking^{24, 25} as well as larger pockets of space^{26, 27}; however, Delaunay tessellation becomes less suitable when a particle cannot be accurately represented by a single point. A set-Voronoi tessellation (Johnson-Mehl tessellation, see **supplementary note 1**) uses entire particles as starting objects to divide the space into pods, where each pod contains an individual particle plus the volume of void space closest to it^{18, 20, 22, 23, 28-30}, and in this way, descriptors of pods can capture information about void space. However, segmenting the space by particle-based pods fractionates the so-called 3-D pores (empty regions of space) of the system. Our initial goal is to segment the void space into subspaces that represent 3-D pores.

Most segmentation methods utilize or derive data from a Euclidean distance transform (EDT) (distance map) over the void space, where the map indicates distance from void space to nearest particle boundary (**supplementary note 2**). These methods often focus on the medial axis (skeleton, backbone) of the space, i.e., points located midway between particles³¹⁻³⁵, and rely on locating the local maxima (peaks) of the EDT, which correspond to local center points in space. Methods for finding the medial axis include: 1) morphological approaches, such as thinning (erosion) algorithms that start at the particle boundaries and erode inward toward the midlines³⁶⁻⁴⁰, 2) crash (shock) detection in wave propagation techniques often based on solving a partial differential equation, including watershed algorithms^{17, 41}, and 3) brute force methods like finding maximally-inscribed spheres whose centers lie along medial axis points^{25, 42, 43}. In general, however, it is nontrivial to accurately locate true peaks in a discretized space. For one, true peaks may lie between grid points. In addition, boundary noise can result in spurious local maxima that do not fit the definition of a peak despite getting classified as one. Morphological approaches, such as morphological reconstruction, or brute force methods that scan for local maxima using gradually increasing window sizes⁴⁴ are prone to miss true peaks and/or identify false ones; however, thresholding or smoothing the data using imaging processing techniques such as Gaussian filters prior to searching helps to minimize this^{40, 45-47}. Regarding the medial axis, particles with even the slightest of boundary fluctuations can produce extraneous branches that extend from the true medial axis toward the non-smooth boundary regions. In this case, auxiliary methods are needed to ‘trim’ or ‘prune’ the extraneous branches^{40, 42, 48, 49}. Although the work-around methods for identifying true peaks can be great options for tackling a difficult problem, they rely on user-selected thresholds that make the outputs only approximations without guarantee for 100% accuracy. Even after peaks are identified, substantial over-segmentation will occur if all peaks are naively used to reference unique subunits^{40, 44} (as in watershed).

We emphasize that our segmentation goal is to extract manageable and *meaningful* subspaces (subunits), and we believe preserving the 3-D pockets of open space is akin to delineating the natural ‘rooms’ of the void space separated by narrow ‘hallways.’ Given that we are interested in how encapsulated or infiltrating cells fit into and interact with the interior of our particle scaffolds, such a segmentation seems natural and fitting.

The Software

To address a shortcoming in the field, we have developed LOVAMAP, a powerful software for visualizing and analyzing 3-D packed particles by first segmenting the void space into 3-D pores (subunits). LOVAMAP was developed and tested on simulated granular scaffolds (particle domains) that exhibit physically accurate phenomena, such as particle jamming (**Figure 1a**), where, unlike with microscope images, useable data is not restricted to a microscope’s depth of field. Since the location of each particle lays the foundation for our methods, LOVAMAP requires a specific input data format (‘labeled’ domains) that highlights individual particles. Each voxel associated with a particular particle must be labeled with the particle’s unique identifying number, and our code can convert sphere data (center and radius) into this format (**Supplementary Figure 1a**). Working with labeled domains ensures that our software is

analyzing exactly what the user intends. **Supplementary Figure 1b,c** provides the workflow for LOVAMAP.

There are five aspects to LOVAMAP that distinguish it from other segmentation software:

1. Euclidean distance transform (EDT) computed for each particle

Instead of computing a single Euclidean distance transform (EDT) of the void space to extract the medial axis, we compute the EDT for each particle as a way to store how many particles are equidistant to a voxel, as well as which particles are equidistant. We store this cumulative EDT information at each voxel (**Figure 1b**), employing various algorithmic optimizations to minimize memory and computational overhead. This approach also accommodates non-smooth particles and, notably, removes the need for pruning the medial axis. Performing this step provides us with the data necessary for identifying medial axis subtypes using the particle configuration, which is a method that we term MAPC.

2. Medial axis by particle configuration (MAPC)

The particle configuration itself (neighboring-particles graph) serves as the basis for our segmentation approach, and we term this approach MAPC, which stands for ‘medial axis by particle configuration.’ Elements of each medial axis subtype (2D-ridges, 1D-ridges, and peaks, **Figure 1c**) are uniquely defined by their equidistant particles. Briefly, 2D-ridges comprise points that are equidistant to precisely two particles, 1D-ridges are located at intersections of 2D-ridges, and peaks are located at intersections of 1-D ridges. The 2D- and 1D- tags refer to the surfaces (2-manifolds) and curves (1-manifolds), respectively, that are formed by these spatial landmarks in a 3-D domain, while the terms ‘ridge’ and ‘peak’ describe the look of the landmarks in a plot of 2-D EDT data (**Figure 1b**). MAPC assigns to each medial axis point an ‘ID’ number that is related to its equidistant particles. This information can then be used to associate points that belong to the same unique element of a given subtype. MAPC makes LOVAMAP specifically designed for granular material.

3. Set of smallest loops in neighboring-particles graph to locate 1D-ridges

We are able to determine the existence and location of all unique 1D-ridges in our space by finding the set of smallest loops in the neighboring-particle graph. We recognize that this set of particle loops defines all unique 1D-ridges in the scaffold, which means we can identify all 1D-ridges according to the particle configuration. This makes our novel approach independent from the grid. **Figure 1d** shows a sample loop defining a ridge that is equidistant to particles ρ_1 , ρ_2 , and ρ_3 . According to MAPC, these points are assigned the unique ID number (1, 2, 3), which defines this 1D-ridge. Our method for finding the set of smallest loops was adapted from the novel approach by Lee et al.⁵⁰

4. Multiple peaks in a single subunit

Fourth, we avoid over-segmentation by associating peaks that belong to the same open space. Unlike classic segmentation approaches that use every local center point to uniquely define void space subunits (as in watershed), we form subunits that can contain multiple center points. In this way, our segmentation approach captures the natural pockets of open space, where these pockets can be thought of as rooms (subunits) separated by doors. To identify which peaks belong to the same room, we check if the physical distance between peaks is less than the sum of their EDT values (see **Methods** for rationale). We prefer the non-parametric nature of this approach that only uses information about the space itself. Similar logic has been used to prune peaks or identify large channels of space^{37, 38, 47}. Sets of linked peaks are used to define unique subunits for void space segmentation (**Figure 1e**) and associated 1D-ridges of linked peaks form their backbone (**Figure 1f**). A nearest neighbors algorithm applied to each backbone is used to complete the segmentation and form 3-D volumes of void space subunits (**Figure 1g**). Unlike subunits derived from over-segmentation (**Figure 1h**), our subunits capture the intrinsic pockets of empty space in the scaffold (**Figure 1i**), which provides more useful subspace data for cell behavior studies.

For a data output comparison between LOVAMAP and over-segmentation, see **Supplementary Figure 2**.

5. Segmenting the entrances and exits of scaffolds

Fifth, we capture true open pockets of space from all perspectives – both entering / exiting the scaffold as well as moving around the interior. Other segmentation approaches extend void space segmentation boundaries to the surface of the void space, which breaks apart the natural openings into the scaffold as viewed by an infiltrating cell (**Figure 1j**). To address this, we segment the 2D-surface of the void space as a separate entity (**Supplementary Figure 1c**), then combine 2D-surface segmentation with interior segmentation to form the final void space subunits (**Figure 1k**). Including this step is essential for isolating true 3-D pores as defined by open pockets of interconnected space separated by narrow channels.

6. Simulating non-rigid, non-smooth, non-spherical particles and visualizing void space

As a bonus sixth, we highlight two notable aspects of the work that are not part of LOVAMAP itself: 1) Our work utilizes powerful animation software to generate simulated granular scaffolds that comprise more sophisticated particles than standard spheres, such as soft-body particles, rough particles, and non-spherical particles (**Figure 1l**). The last panel in **Figure 1l** showcases how we can generate non-standard particle domains inspired by real MAP scaffolds. 2) Our figures exemplify how LOVAMAP data can be used to visualize 3-D pores and characterization metrics. These images are important for data visualization and science communication.

The Descriptors

LOVAMAP-1.0.0 outputs 44 descriptors that are categorized as either global, subunit, or interunit. A global descriptor is a single value that describes a scaffold, a subunit (pore) descriptor reports a distribution of measurements over each subunit in a scaffold, and an interunit descriptor is a distribution of measurements over non-subunit elements. **Table 1** lists all descriptors, which are further organized by subcategories to motivate their utility. These motivations cover topics such as void space connectivity, subunit size, shape and directionality, ligand availability, and movement through the void space.

Void space connectivity

As inspiration for developing descriptors to address void space connectivity, we first envisioned cells that are seeded within our MAP scaffolds and that reside in the void space, as seen by our lab and others². These cells explore and traverse the space that is available to them without degrading the scaffold. We began by studying doors and hallways of packed rigid particles, where doors lie at partitions between subunits (**Figure 2a**) and hallways pass through doors along 1D-ridges that are shared between subunits (**Figure 2b**). We report the diameter of doors across the scaffold, as well as the number of hallways per subunit, which is also referred to as the subunit's coordination number (**supplementary note 3**). For a given subunit, its 'hallway' neighbors comprise a subset of a larger set of adjacent subunits (rooms) that share 2D-ridges (**Figure 2c**). Therefore, some but not all adjacent rooms will share a door (1D-ridge) with the subunit. Lastly, we include the eigenvalue of three adjacency matrices (particle, peak, and subunit) to provide more abstract descriptors of interconnectivity (**Supplementary Figure 3; supplementary note 4**). The eigenvalue for each descriptor is bounded below by the average number of edges per node and bounded above by the maximum number of edges amongst all nodes.

Subunit size, shape, and directionality

LOVAMAP outputs classic descriptors, such as volume and characteristic length; however, to address size restrictions, we output both the largest enclosed sphere (**Figure 2d**), as well as the smallest door per subunit. We approximate an ellipsoid for each subunit using principal component analysis (PCA) (**Figure 2e** left), then report the length of the ellipsoid in each direction to understand the spread of the shape (**supplementary note 5**). To capture more topographical detail, we also compute mean local

thickness for each subunit, which is a measurement adapted from Hildebrand and Ruegsegger⁵¹. Mean local thickness uses enclosed spheres within the subunit to assign local thickness measurements that are then averaged. A sphere of diameter d has a mean local thickness equal to d ; however, a cube with height d has a mean local thickness that is less than d because local thickness decreases toward the corners of the cube, which brings down the average (**supplementary note 6**). We also capture topographical complexity by reporting the number of 2D-ridges within a subunit because the location of 2D-ridges correlates with the number of vertices (or tips) along the surface of the subunit (**Figure 2f**).

Since granular scaffolds are utilized as tissue mimics, we are interested in an isotropy / anisotropy measurement of void space that reflects the entire scaffold – similar to the way collagen fiber orientation is described for scar assessment⁵². To do so, we study the relative orientation of each pocket of void space, which uses eigenvectors from the subunit ellipsoids derived from PCA (**Figure 2e** right) (see **Methods** for details). Our unitless isotropy-anisotropy descriptor ranges between 0 and 1, and a uniform distribution of the descriptor suggests anisotropy.

Ligand availability

Granular scaffolds often comprise particles that are designed with surface ligands to attract cells (**Figure 2g i**), so we use experimental data to assign ligand molecules to particle shells. For each void space subunit, we locate particle surfaces that enclose the pocket of space to compute ‘accessible ligand’ (in μ moles) per subunit (**Figure 2g ii**). We also compute this for the openings into and out of the scaffold (**Figure 2g iii**). Next, we create a ligand heatmap by using an averaging filter in order to mimic the average number of ligand molecules sensed by a migrating 10 μ m spherical cell (**Figure 2g iv**). Our results allow us to compute the volume fraction of ligand ‘hotspots’ within the scaffold (**Figure 2g v**), as well as the ligand concentration (in μ moles / L) per subunit and per scaffold opening that is sensed by residing and infiltrating cells, respectively (**Figure 2g vi,vii**).

Movement through void space

We next consider how the size of an object impacts where it can travel within the void space. We study four spherical object species of varying diameters: molecules (< 1 μ m), cells (10 μ m), 3-cell clusters (30 μ m), and 6-cell clusters (60 μ m). For each object, we map out all distinct regions of the void space where the object can fit. **Figure 2h** gives a visual representation for a 40- and 100-diameter rigid particle domain, where distinct regions are highlighted by unique colors. An object cannot move between regions, and as an object becomes larger, the available regions become increasingly disjoint and sparse. To capture this phenomenon, we report the volume of each region of space that can contain the object.

Lastly, to study available routes for an infiltrating object or flow through the scaffold, we define a path as the shortest route along the 1D-ridge backbone from the center of the scaffold to an entrance-exit door (**Figure 2i,j**). By computing paths to each entrance, we produce path descriptors that include path length, as well as two measurements of tortuosity (**Figure 2k**). Tortuosity-by-length refers to the arc-chord ratio, the simplest definition of tortuosity (**supplementary note 7**), while tortuosity-by-volume refers to the volume of the convex hull containing the set of path points. Unlike arc-chord ratio, a volume-based approach for describing tortuosity will scale with path size. An output comparison between the two metrics is presented in **Supplementary Figure 4**.

Data Analysis

Library of granular scaffold standards

We have created a diverse library of packed particle ‘standards’ to be used as a reference in the field, boasting over 60 scaffold types and over 400 descriptor data plots comparing them. Our library includes scaffolds comprising random-packing of homogeneous rigid spheres, heterogeneous rigid spheres, homogeneous soft-body spheres, binary mixtures of rigid and soft-body spheres, non-smooth spheres,

and non-spherical particles, as well as square and hexagonal perfect-packing to serve as controls. To accompany our data library, we provide sample images of different simulated scaffolds and their corresponding subunits, which helps users to appreciate the variation in 3-D pore size and shape that accompanies changes in particle composition (**Figure 3a-h**). Cumulatively, our plots contain descriptor data from over 550 particle domains and serve as an easy look-up (**Supplementary Data 1-29**). For those interested in more detail, we provide the raw descriptor data for each plot, as well as the distribution measurements (e.g., mean, median, mode, etc.) for non-global descriptors. Our library of standards is a great resource for granular scaffold engineers.

What is a 'pore,' and how can it be measured?

In the context of granular scaffolds, 'pores' refer to the open pockets of space throughout the scaffold, and LOVAMAP provides a deterministic approach for extracting 3-D pores, i.e., subunits. In the field, the pore size of granular scaffolds is frequently approximated using 2-D z-slice images, where areas of void islands are reported after binarizing and thresholding^{9, 53-57} or measurements are taken using lines that are manually fit within regions of 2-D void space. To highlight the importance of studying 3-D space, we compare pore size using the diameters of largest enclosed circles vs. largest enclosed spheres for void pockets in 2-D slices vs. 3-D subunits, respectively (**Figure 3i**). For rigid, semi-soft, and soft 100 μm diameter particle domains, we see that approximating pore diameter using 2-D slice data tends to underestimate pore size and result in wider variation in the data compared to the more accurate 3-D approximations used in LOVAMAP (**Figure 3j**). These trends are more extreme for rigid particle domains, and they lessen as particles become soft and overall void space reduces (**Supplementary Figure 5**). This data suggests that while 2-D analysis serves as an easy first-pass approximation for pore diameter, largest enclosed sphere diameter is more accurate for representing true pore dimension.

Yet still, a single descriptor is not enough to capture the spatial complexity of a pore, which can be visually appreciated in **Figure 1g** and **Figure 3a-h**. LOVAMAP aims to tackle this challenging problem by describing a pore with 17 measurements (**Table 1**, Subunit). The variation across subunit descriptor data for specific domains speaks to the complexity of pore space (**Supplementary Data 2,6,10,12,15,19,23,27**).

Confirming isotropy / anisotropy of void space

As mentioned previously, each void subunit is assigned an isotropy / anisotropy measurement between 0 and 1 that reflects the orientation of its PCA ellipsoid relative to the average orientation. If the collective subunit orientations are random, the resulting distribution will follow a uniform distribution with a lower bound of 0 and an upper bound of 1, which suggests an anisotropic scaffold with respect to the void space. To validate our isotropy / anisotropy descriptor, we generated a special set of rigid ellipsoid domains with varying levels of particle alignment (**Figure 3k**). We hypothesized that the inherent directionality of ellipsoids would contribute to directionality of void space subunits and that more aligned (isotropic) ellipsoids would produce isotropic subunits. As a control, we compare against 60 μm diameter rigid spheres in random packing since a collection of spherical particles inherently does not exhibit alignment due to radial symmetry of the particle shape. As expected, the resulting subunits from spherical particles exhibited anisotropy (**Figure 3l**). Ellipsoids in random packing (anisotropic) produced a distribution that is weakly skewed; however, we see a drastic shift for aligned ellipsoids, which generated a heavily skewed distribution (**Figure 3l**). This result is a clear indication that void space pockets are aligned in a similar direction for this domain and can therefore be classified as isotropic. The validity of our metric is confirmed with square packing of ellipsoids in which all subunits are pointing in the same direction, producing a shifted Dirac delta distribution, which is non-uniform between 0 and 1 (**Figure 3l**). Images of PCA ellipsoids and major axes vectors for each domain are shown in **Supplementary Figure 6**.

Pore 'types' and granular scaffold 'fingerprints'

LOVAMAP subunit data can be used to identify void space pocket ‘types’ using higher dimensional analysis. By running t-distributed stochastic neighbor embedding (tSNE) on scaffold subunits that are labeled by their 17 subunit descriptors, we can identify clusters of similar subunits (**Figure 4a**). Subunits from a given cluster reference a subunit type, and descriptor labels define the type. We showcase subunits from sample clusters to appreciate visual similarities in size and shape (**Figure 4a** right). tSNE can also be used to compare the subunits from one scaffold against the subunits found in an array of scaffold standards (**Figure 4b-d**). For example, we can verify that packing soft particles creates void space pockets that are not found in rigid particle scaffolds, regardless of the particle size (**Figure 4b**). Interestingly, these subunit types can be seen in scaffolds made from nugget- and rod-shaped particles. Despite the random nature of packed particles, our analysis reveals that there are underlying patterns to the local geometry of void space across scaffold standards generated under similar conditions. Therefore, if researchers are interested in designing granular scaffolds with a specific void pocket geometry, LOVAMAP allows them to do so more confidently than before.

LOVAMAP data can also serve as a numeric ‘fingerprint’ of scaffold types. This time, we use information from all descriptors to label each scaffold, and we look at which scaffolds cluster with one another (**Figure 4e**). When we include a real MAP scaffold containing ~100 μm diameter microgels against all scaffold standards, we see that our real MAP scaffold clusters with the simulated scaffold containing homogeneous soft 100 μm particles. This result provides evidence that it is possible to characterize MAP scaffolds using a fingerprint defined by descriptors.

Real MAP scaffolds

In a recent publication investigating the ability of MAP scaffolds to control neuronal progenitor cell (NPC) differentiation, our lab found conditions in which neurosphere formation occurred in the void space of MAP scaffolds⁵⁸. Neurospheres have a long history as both *in vitro* models for studying neurogenesis and neurodegenerative diseases and as organoid precursors⁵⁹. In the aforementioned publication, we used standard methods such as gene expression, ELISA, and immunofluorescence to assess NPC differentiation and neurosphere formation. However, we had no direct way of studying how the underlying microarchitecture of our granular scaffolds impacted NPCs.

With the development of LOVAMAP, we can now explore the relationship between NPCs and void space by analyzing microscope images from this study that display neurospheres in MAP one week after neuronal progenitor cells were seeded *in vitro* (**Figure 4a**). The neurosphere condition was a natural place to start because we found that spread cells exerted a contractile force that moved the microgels and led to changes in the void over time, while neurospheres did not⁵⁸. We ran LOVAMAP on six MAP scaffold samples, which required first converting the microscope images into labeled domain format using code previously described in¹⁴. The same code was also used to extract neurosphere data (**Figure 4b**). We opted to forgo combining edge subunits that share scaffold openings due to the thin nature of the samples, so our segmentation represents 3-D pores from the perspective of the interior only (**Figure 4c**). **Figure 4d** highlights void space subunits that house neurospheres.

To start our analysis, we compare MAP scaffolds against standards from our library of scaffolds and also highlight subunits that contain neurospheres. We find that MAP subunits appear to be more similar, on average, to simulated domains containing semi-soft particles compared to rigid and soft particles, but with greater variation (**Figure e-h**, **Supplementary Figure 7**). Such variability can be attributed to sources such as microscope image quality and image processing steps during segmentation. When we overlay descriptor data from subunits containing neurospheres, we see that neurospheres tend to reside in larger spaces (**Figure e,f**). If we relate 3-D pore connectivity and complexity to the number of subunit hallways and peaks, respectively, we see that these metrics play little role in dictating where neurospheres form (**Figure g,h**). To explore the influence of subunit size further, we focus on subunits that contain neurospheres, and we look at two metrics: total volume (μL) and the volume of the largest

enclosed sphere (pL) (**Figure i**). As expected, subunit volumes are consistently larger than their largest enclosed sphere. However, our results show remarkable similarity between the distributions of largest enclosed sphere and neurosphere volume. This result indicates that neurosphere size is dictated by the maximum local space available for a sphere to grow.

We next observe where neurospheres form by studying void space landmarks. On average, our results suggest that neurospheres are more often found at local center points in space (peaks) compared to the narrow regions that separate open spaces (doors) (**Figure j**) (p -value 0.0558). This further supports the notion that neuronal progenitor cells in MAP scaffolds form neurospheres in larger, open pockets of void space. Neurospheres at doors likely represent neurosphere movement between subunits, which has been shown to occur⁵⁸, so our data could be used as a metric for this phenomenon.

To capture a deeper complexity about what void space features drive neurosphere formation, we run tSNE on subunits from our MAP scaffolds (**Figure k**). The tSNE plot reveals a cluster that contains a predominance of neurospheres, so we extract these subunits to observe the features that distinguish them. This cluster, i, represents some of the largest subunits, as indicated by descriptors such as largest enclosed sphere (pL), volume (pL), and mean local thickness (μm) (**Figure 5k** cluster i, **Supplementary Figure 34**). In contrast, when we extract subunits from the cluster containing the fewest neurospheres, cluster ii, we find that these subunits represent some of the smallest spaces in the scaffolds, as indicated by largest enclosed sphere and other descriptors that capture pore size (**Figure 5k** cluster ii, **Supplementary Data 35**). However, these small subunits in particular have additional distinguishing features – they are like narrow tubes of varying lengths. This is described by the PCA ellipsoid descriptors that show small values for the length of ellipsoid axis 2 and 3, while the principal axis appears randomly distributed (**Figure 5k** cluster ii, **Supplementary Figure 35**). Our results indicate that neuronal progenitor cells will avoid forming neurospheres in small, narrow, tubes of space. Lastly, we highlight a third distinct cluster, iii, that contains neurospheres. These subunits represent a very specific subunit ‘type,’ with precise values for many descriptors, including those that represent size as well as those that capture information about subunit vertices (tips) (**Figure 5k** cluster iii, **Supplementary Figure 36**). These results showcase the ability of LOVAMAP to identify different types of 3-D pores in granular scaffolds, which can be used in conjunction with neurosphere data to help us understand how void space geometry dictates neurosphere formation in MAP scaffolds.

Conclusion

For any field working with packed particle systems, we recommend LOVAMAP – a one-of-a-kind software for studying and visualizing void space microarchitecture. LOVAMAP is specially suited for segmenting out the 3-D pores (subunits) of granular scaffolds using clever techniques, such as MAPC, to locate important spatial landmarks in the void space. Using LOVAMAP, we have created a library of over 60 simulated scaffold standards with accompanying data that spans topics such as pore size, shape, connectivity, directionality, ligand availability, void space availability by cell size, paths, and openings into and out of the scaffold. We demonstrate how higher dimensional analysis of LOVAMAP outputs can be used to classify types of 3-D pores, as well as types of granular scaffolds, where LOVAMAP descriptors are used as numeric identifiers that define different ‘types.’ Such analysis has been used to study real MAP scaffolds that contain neurospheres, and our work corroborates the notion that neurosphere growth is dictated in part by the largest enclosed sphere of large, wide 3-D pores. Results show that small, tube-like void spaces are not conducive to neurosphere formation. In conjunction with running LOVAMAP on future scaffolds, this information not only helps to inform scaffold design toward guiding the size and location of neurosphere formation, but additionally, our work exemplifies how a single descriptor, such as void volume fraction or 2-D pore area, alone cannot characterize the complexity of void space.

Moving forward, we will continue to add to LOVAMAP's functionality and expand our statistical approaches for data analysis. In collaboration with Ninjabyte Computing (**supplementary note 8**), we aim to generate a library of soft-body particle domains with corresponding Lamé parameters for easy look-up and use, as well as incorporate additional scaffold features into our simulations, such as viscous fluid, particle interlinking prior to settling, and ranging particle-packing density. For analyzing microscope images of packed particles, we will focus on improving 3-D particle segmentation, which is used to generate labeled particle domains, since the accuracy of inputs will affect the accuracy of outputs. For LOVAMAP, we are motivated to develop more sophisticated curvature measurements because studies have shown relationships between surface curvature and cell stress, which drives a number of cell phenomena including growth¹¹. Studying subunit vertices in more depth may reveal additional information about curvature⁶⁰. LOVAMAP descriptor data can also be used to study macroscale material properties²⁸. As part of our statistical exploration, we will investigate higher moments to further characterize descriptor distributions. For higher dimensional analysis, machine learning algorithms can be implemented to identify the most influential descriptors for a given MAP scaffold.

Author contributions

LR headed the development of the work by designing the computational framework, writing and implementing novel code, generating data, analyzing data, writing the manuscript, and creating figures. PC provided computational expertise through guidance and discussion, contributed to the design of the computational framework, wrote novel code, played a key role in improving software runtime speeds, designed and simulated input domains, contributed to writing methods, and organized the flow of the final manuscript. TS was pivotal in the conception and direction of the project, including applications to real data, provided guidance and discussion throughout, and made substantial contribution to data analysis, figure preparation, and manuscript organization and editing.

Acknowledgements

We would like to thank the National Institutes of Health, the National Institutes of Neurological Disorders and the Stroke (1R01NS112940, 1R01NS079691, R01NS094599), and the National Institute of Allergy and Infectious Disease (1R01AI152568). Thank you to Katrina Wilson, a fellow Segura Lab member, for providing the MAP scaffold microscope images containing neurospheres. Thank you to Yijun Bao, PhD and Professor Yiyang Gong at Duke University for providing the code to convert the real microscope images of MAP scaffolds into labeled particle domains. We extend a special thanks to Mahdi Roozbahani, PhD, who was a senior graduate student under Professor David Frost at Georgia Tech when he kindly shared his experience and expertise during the early stages of the project. Thank you to Eric Monsoon in the Center for Data and Visualization Science at Duke University for his time and input.

Data availability

Raw datasets as well as distribution measurements used to generate tSNE domain plots can be downloaded at <https://seguralab.duke.edu/what/highlights/lovamap/#look-up>.

Code availability

The copyrights of the LOVAMAP software are owned by Duke University. Developed by Lindsay Riley, Peter Cheng, and Tatiana Segura at the Segura Lab, Duke University Pratt School of Engineering. To request a license to this software, please contact the Digital Innovations department at the Duke Office for Translation & Commercialization (OTC) (<https://olv.duke.edu/software/>) at otcquestions@duke.edu with reference to 'OTC File No. 7784'.

Please note that this software is distributed AS IS, WITHOUT ANY WARRANTY; and without the implied warranty of MERCHANTABILITY or FITNESS FOR A PARTICULAR PURPOSE.

References

1. Riley, L., Schirmer, L. & Segura, T. Granular hydrogels: emergent properties of jammed hydrogel microparticles and their applications in tissue repair and regeneration. *Curr Opin Biotechnol* **60**, 1-8 (2019).
2. Daly, A.C., Riley, L., Segura, T. & Burdick, J.A. Hydrogel microparticles for biomedical applications. *Nat Rev Mater* **5**, 20-43 (2020).
3. Darling, N.J. et al. Click by Click Microporous Annealed Particle (MAP) Scaffolds. *Adv Healthc Mater* **9**, e1901391 (2020).
4. Fang, J. et al. Injectable Drug-Releasing Microporous Annealed Particle Scaffolds for Treating Myocardial Infarction. *Adv Funct Mater* **30** (2020).
5. Griffin, D.R. et al. Activating an adaptive immune response from a hydrogel scaffold imparts regenerative wound healing. *Nat Mater* **20**, 560-569 (2021).
6. Dumont, C.M. et al. Aligned hydrogel tubes guide regeneration following spinal cord injury. *Acta Biomater* **86**, 312-322 (2019).
7. Griffin, D.R., Weaver, W.M., Scumpia, P.O., Di Carlo, D. & Segura, T. Accelerated wound healing by injectable microporous gel scaffolds assembled from annealed building blocks. *Nat Mater* **14**, 737-744 (2015).
8. Truong, N.F. et al. Microporous annealed particle hydrogel stiffness, void space size, and adhesion properties impact cell proliferation, cell spreading, and gene transfer. *Acta Biomater* **94**, 160-172 (2019).
9. Matsiko, A., Gleeson, J.P. & O'Brien, F.J. Scaffold mean pore size influences mesenchymal stem cell chondrogenic differentiation and matrix deposition. *Tissue Eng Part A* **21**, 486-497 (2015).
10. McWhorter, F.Y., Wang, T., Nguyen, P., Chung, T. & Liu, W.F. Modulation of macrophage phenotype by cell shape. *Proc Natl Acad Sci U S A* **110**, 17253-17258 (2013).
11. Zadpoor, A.A. Bone tissue regeneration: the role of scaffold geometry. *Biomater Sci* **3**, 231-245 (2015).
12. Denais, C.M. et al. Nuclear envelope rupture and repair during cancer cell migration. *Science* **352**, 353-358 (2016).
13. Werner, M. et al. Surface Curvature Differentially Regulates Stem Cell Migration and Differentiation via Altered Attachment Morphology and Nuclear Deformation. *Adv Sci (Weinh)* **4**, 1600347 (2017).
14. Riley, L. et al. Void volume fraction of granular scaffolds. *bioRxiv* (2022).
15. Ketcham, R.A., Meth, C., Hirsch, D.M. & Carlson, W.D. Improved methods for quantitative analysis of three-dimensional porphyroblastic textures. *Geosphere* **1** (2005).
16. Videla, A., Lin, C.-L. & Miller, J.D. Watershed Functions Applied to a 3D Image Segmentation Problem for the Analysis of Packed Particle Beds. *Particle & Particle Systems Characterization* **23**, 237-245 (2006).
17. Doerr, F.J.S. & Florence, A.J. A micro-XRT image analysis and machine learning methodology for the characterisation of multi-particulate capsule formulations. *Int J Pharm X* **2**, 100041 (2020).
18. Corwin, E.I., Clusel, M., Siemens, A.O.N. & Brujić, J. Model for random packing of polydisperse frictionless spheres. *Soft Matter* **6** (2010).
19. Walker, D.M. et al. Self-assembly in a near-frictionless granular material: conformational structures and transitions in uniaxial cyclic compression of hydrogel spheres. *Soft Matter* **11**, 2157-2173 (2015).

20. Zhao, S., Evans, T.M. & Zhou, X. Three-dimensional Voronoi analysis of monodisperse ellipsoids during triaxial shear. *Powder Technology* **323**, 323-336 (2018).
21. Yi, L.Y., Zou, R.P., Pinson, D., Dong, K.J. & Yu, A.B. An assessment of the mathematical models for estimating the coordination number of the packing of multisized particles. *Powder Technology* **379**, 58-68 (2021).
22. Zhang, C., Zhao, S., Zhao, J. & Zhou, X. Three-dimensional Voronoi analysis of realistic grain packing: An XCT assisted set Voronoi tessellation framework. *Powder Technology* **379**, 251-264 (2021).
23. Zhao, S., Zhao, J. & Guo, N. Universality of internal structure characteristics in granular media under shear. *Phys Rev E* **101**, 012906 (2020).
24. Natsui, S., Sawada, A., Nogami, H., Kikuchi, T. & Suzuki, R.O. Topological Consideration of 3-D Local Void Structure for Static Holdup Site in Packed Bed. *ISIJ International* **60**, 1453-1460 (2020).
25. Shelepova, E.A., Paschek, D., Ludwig, R. & Medvedev, N.N. Comparing the void space and long-range structure of an ionic liquid with a neutral mixture of similar sized molecules. *Journal of Molecular Liquids* **299** (2020).
26. Li, Z., Wang, Y.H., Chow, J.K., Su, Z. & Li, X. 3D pore network extraction in granular media by unifying the Delaunay tessellation and maximal ball methods. *Journal of Petroleum Science and Engineering* **167**, 692-701 (2018).
27. van der Linden, J.H., Sufian, A., Narsilio, G.A., Russell, A.R. & Tordesillas, A. A computational geometry approach to pore network construction for granular packings. *Computers & Geosciences* **112**, 133-143 (2018).
28. Li, X. & Li, X.S. Micro-Macro Quantification of the Internal Structure of Granular Materials. *Journal of Engineering Mechanics* **135**, 641-656 (2009).
29. Schaller, F.M. et al. Non-universal Voronoi cell shapes in amorphous ellipsoid packs. *EPL (Europhysics Letters)* **111** (2015).
30. Weis, S., Schönhöfer, P.W.A., Schaller, F.M., Schröter, M. & Schröder-Turk, G.E. Pomelo, a tool for computing Generic Set Voronoi Diagrams of Aspherical Particles of Arbitrary Shape. *EPJ Web Conf.* **140**, 5-8 (2017).
31. Blum, H. in *Models for the Perception of Speech and Visual Form* 363-380 (1967).
32. Sherbrooke, E.C., Patrikalakis, N.M. & Brisson, E. An Algorithm for the Medial Axis Transform of 3D Polyhedral Solids. *IEEE TRANSACTIONS ON VISUALIZATION AND COMPUTER GRAPHICS* **2**, 44-61 (1996).
33. Pizer, S.M., Siddiqi, K., Székeley, G., Damon, J.N. & Zucker, S.W. Multiscale medial loci and their properties. *International Journal of Computer Vision* **55**, 155-179 (2003).
34. Hesselink, W.H. & Roerdink, J.B.T.M. Euclidean skeletons of digital image and volume data in linear time by the integer medial axis transform. *IEEE Transactions on Pattern Analysis and Machine Intelligence* **30**, 2204-2217 (2008).
35. Xiong, Q., Baychev, T.G. & Jivkov, A.P. Review of pore network modelling of porous media: Experimental characterisations, network constructions and applications to reactive transport. *J Contam Hydrol* **192**, 101-117 (2016).
36. Chiang, S.-C. 177 (Purdue University, 1992).
37. Liang, Z., Ioannidis, A. & Chatzis, I. Geometric and Topological Analysis of Three-Dimensional Porous Media: Pore Space Partitioning Based on Morphological Skeletonization. *Journal of Colloid and Interface Science* **221**, 13-24 (2000).
38. Youssef, S. et al. in *All Days* (2007).
39. Thomson, P.-R., Hazel, A. & Hier-Majumder, S. The Influence of Microporous Cements on the Pore Network Geometry of Natural Sedimentary Rocks. *Frontiers in Earth Science* **7** (2019).
40. Jones, A.C. et al. The correlation of pore morphology, interconnectivity and physical properties of 3D ceramic scaffolds with bone ingrowth. *Biomaterials* **30**, 1440-1451 (2009).

41. Rabbani, A., Ayatollahi, S., Kharrat, R. & Dashti, N. Estimation of 3-D pore network coordination number of rocks from watershed segmentation of a single 2-D image. *Advances in Water Resources* **94**, 264-277 (2016).
42. Silin, D. & Patzek, T. Pore space morphology analysis using maximal inscribed spheres. *Physica A: Statistical Mechanics and its Applications* **371**, 336-360 (2006).
43. Huaimin, D., Jianmeng, S., Likai, C., Naser, G. & Weichao, Y. Characteristics of the pore structure of natural gas hydrate reservoir in the Qilian Mountain Permafrost, Northwest China. *Journal of Applied Geophysics* **164**, 153-159 (2019).
44. Roozbahani, M.M., Borela, R. & Frost, J.D. Pore Size Distribution in Granular Material Microstructure. *Materials (Basel)* **10** (2017).
45. Jones, J.R., Atwood, R.C., Poologasundarampillai, G., Yue, S. & Lee, P.D. Quantifying the 3D macrostructure of tissue scaffolds. *J Mater Sci Mater Med* **20**, 463-471 (2009).
46. Bashoor-Zadeh, M., Baroud, G. & Bohner, M. Geometric analysis of porous bone substitutes using micro-computed tomography and fuzzy distance transform. *Acta Biomater* **6**, 864-875 (2010).
47. Gostick, J.T. Versatile and efficient pore network extraction method using marker-based watershed segmentation. *Phys Rev E* **96**, 023307 (2017).
48. Shaked, D. & Bruckstein, A.M. Pruning Medial Axes. *Computer Vision and Image Understanding* **69**, 156-169 (1998).
49. Lindquist, W.B. & Venkatarangan, A. Investigating 3D Geometry of Porous Media from High Resolution Images. *Phys. Chem. Earth (A)* **25**, 593-599 (1999).
50. Joon Lee, C., Kang, Y.-M., Cho, K.-H. & No, K.T. A robust method for searching the smallest set of smallest rings with a path-included distance matrix. *PNAS* **106**, 17355–17358 (2009).
51. Hildebrand, T. & Ruegsegger, P. A new method for the model independent assessment of thickness in three dimensional images. *Journal of Microscopy* **185**, 67-75 (1997).
52. Khorasani, H. et al. A quantitative approach to scar analysis. *Am J Pathol* **178**, 621-628 (2011).
53. Muir, V.G., Qazi, T.H., Shan, J., Groll, J. & Burdick, J.A. Influence of Microgel Fabrication Technique on Granular Hydrogel Properties. *ACS Biomater Sci Eng* **7**, 4269-4281 (2021).
54. Caldwell, A.S., Campbell, G.T., Shekuro, K.M.T. & Anseth, K.S. Clickable Microgel Scaffolds as Platforms for 3D Cell Encapsulation. *Adv Healthc Mater* **6** (2017).
55. Sideris, E. et al. Particle Hydrogels Based on Hyaluronic Acid Building Blocks. *ACS Biomater Sci Eng* **2**, 2034-2041 (2016).
56. Sheikhi, A. et al. Microfluidic-enabled bottom-up hydrogels from annealable naturally-derived protein microbeads. *Biomaterials* **192**, 560-568 (2019).
57. Qazi, T.H. et al. Anisotropic Rod-Shaped Particles Influence Injectable Granular Hydrogel Properties and Cell Invasion. *Adv Mater*, e2109194 (2021).
58. Wilson, K.L., Leshner Pérez, S.C., Naffa, M.M., Kelly, S.H. & Segura, T. Stoichiometric post modification of hydrogel microparticles dictates neural stem cell fate in microporous annealed particle scaffolds. *Advanced Materials Accepted* (2022).
59. da Silva Siqueira, L., Majolo, F., da Silva, A.P.B., da Costa, J.C. & Marinowic, D.R. Neurospheres: a potential in vitro model for the study of central nervous system disorders. *Mol Biol Rep* **48**, 3649-3663 (2021).
60. Raeini, A.Q., Bijeljic, B. & Blunt, M.J. Generalized network modeling: Network extraction as a coarse-scale discretization of the void space of porous media. *Phys Rev E* **96**, 013312 (2017).

Figures

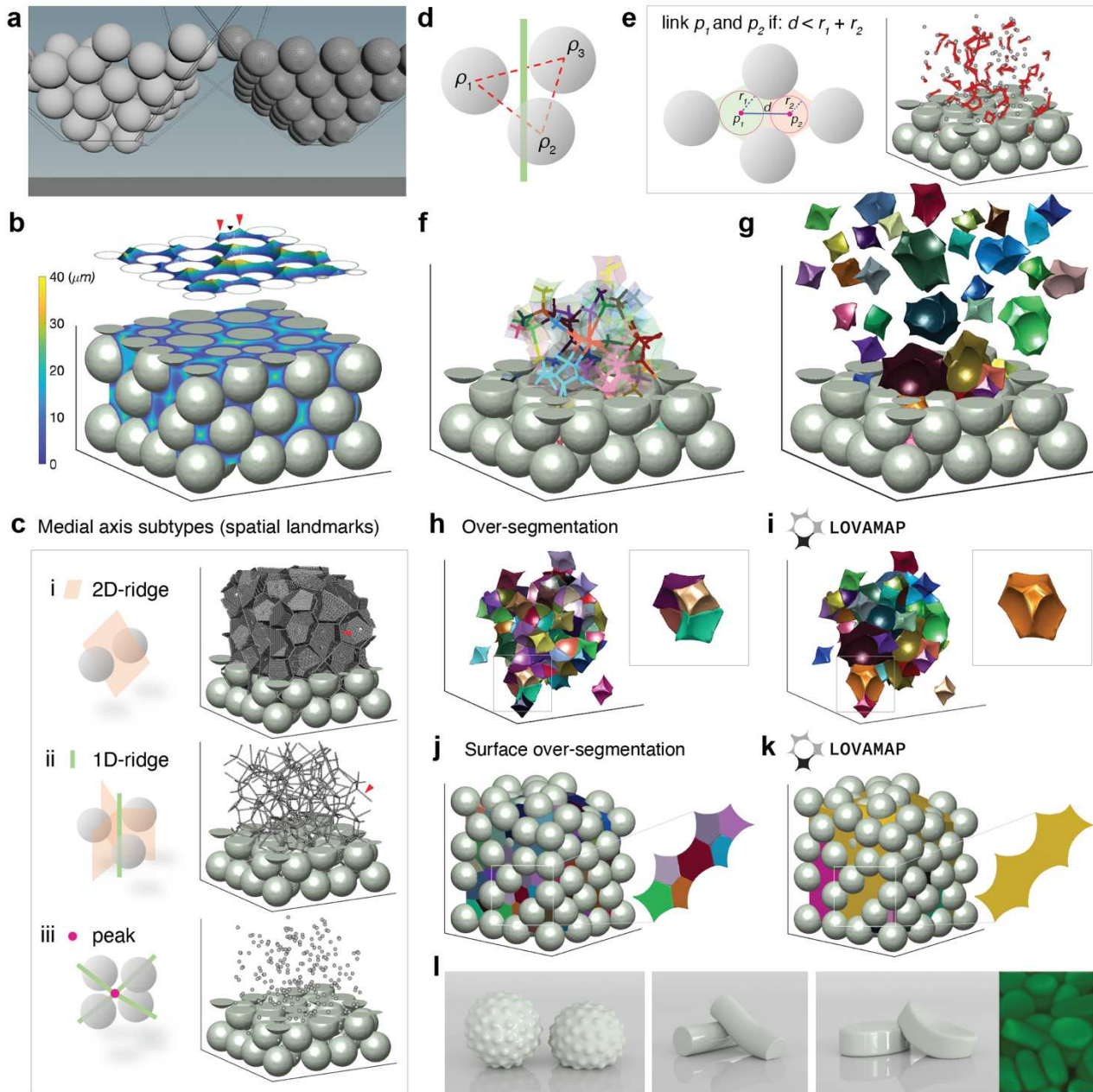


Figure 1 | LOVAMAP software locates 3-D pores (subunits) of granular scaffolds by accurately identify important spatial landmarks of the void space. a, Physically-realistic simulations of particle packing used for software development. Rigid spheres (left) and soft spheres (right) exhibit particle jamming dependent upon the size of the opening. **b**, Heatmap representation of the Euclidean distance transform (EDT) computed on the void space of a scaffold containing 130 μm diameter particles (showing lower half of scaffold), where a z-slice is shown hovering above the scaffold with the EDT plotted in 3-D to reveal the topographical peaks (red arrows) and ridges (black triangle). **c**, Medial axis subtypes. **i**, 2D-ridge points form a surface (2-manifold) between particle pairs. (Right) Unique 2D-ridge indicated by red arrow; **ii**, 1D-ridge points form a curve (1-manifold) at the intersection of 2D-ridges. (Right) Unique 1D-ridge indicated by red arrow; **iii**, peaks are points (0-manifolds) at the intersection of

1D-ridges. **d**, 1D-ridges are physically located within the smallest set of smallest particle loops. Each 1D-ridge (green) is uniquely defined by the set of particles, P , that forms its loop (red dash). $P = \{\rho_1, \rho_2, \rho_3\}$ shown here. **e**, Identifying pockets of open space. Two peaks, ρ_1 and ρ_2 , are considered part of the same open space if the distance, d , between them is less than the sum of their radii, r_1 and r_2 . (Right) Peaks that belong to the same open space are shown linked by 1D-ridges (red). **f**, Void space subunit backbones with transparent subunit volumes. Showing interior subunits only, where interior subunits do not contain backbones that extend to the edge of the scaffold. **g**, Interior void space subunits that are shown separated to appreciate variation in size and shape. **h**, Classic segmentation approaches, e.g., watershed from peaks, result in void space over-segmentation that do not capture the pockets of open space corresponding to 3-D pores. Showing interior void space only. (Right) Over-segmentation of a single 3-D pore. **i**, LOVAMAP segments void space into natural pockets of open space (subunits). Showing interior subunits only. (Right) A single 3-D pore. **j**, Standard segmentation approaches result in over-segmentation of the scaffold openings from an exterior perspective. **k**, LOVAMAP segments the surface (edge) of the scaffold separately, then combines results with interior segmentation to produce void space subunits that represent pockets of open space from both an exterior and interior perspective. **l**, Ninjabite Computing generates sophisticated particles using SideFX Houdini (rendered with Redshift). From left to right, showing rigid and soft versions: rough spheres, rods, nuggets, and the real microscope image that served as our inspiration for nuggets (credit: Sasha Cai, PhD, a former postdoc in the Segura Lab). **Figure b,c,f,g** equivalent images for square and hexagonal packing shown in **Supplementary Figure XX**.

Global	Subunit	Interunit
General Number of particles Void volume fraction Average void area fraction [†] Particle packing fraction Number of subunits Max number of equidistant particles	Size Volume (pL) Surface area ($\mu\text{m}^2 / 1000$) Characteristic length (μm) Number of peaks Largest enclosed sphere diameter (μm) Smallest door diameter (μm)	Particles Particle diameter (μm) Coordination number
Connectivity Number of interior doors Subunit adjacency matrix eigenvalue Peak adjacency matrix eigenvalue Particle adjacency matrix eigenvalue	Shape Ellipsoid axis 1 length (μm) Ellipsoid axis 2 length (μm) Ellipsoid axis 3 length (μm) Mean local thickness (μm) [§] Number of 2D-ridges	Doors Entrance / Exit door diameter (μm) Interior door diameter (μm)
Entrance / Exits Number of exterior doors Max number of peaks among surface subunits Number of paths	Directionality Isotropy / Anisotropy	Paths Path length (μm) Tortuosity-by-length Tortuosity-by-volume (pL)
Ligand availability Ligand hotspots [‡] volume fraction	Connectivity Number of hallways, i.e., coordination number Number of adjacent subunits Normalized Neighbors	Surface Subunits Ligand concentration ($\mu\text{moles} / \text{L}$) Accessible ligand (μmoles)
	Ligand availability Ligand concentration ($\mu\text{moles} / \text{L}$) Accessible ligand (μmoles)	Accessible Regions < 1 μm object region volumes (pL) 10 μm object region volumes (pL) 30 μm object region volumes (pL) 60 μm object region volumes (pL)

[†] The # of evenly-spaced z-slices sampled is a tunable parameter.

[‡] Hotspots are $\geq 2,167,200$ ligand molecules.

[§] Hildebrand T and Rueggsegger P, 1997.

Table 1 | LOVAMAP currently outputs 44 descriptors that are classified into three main types: global, subunit, and interunit. A global descriptor is a single measurement over the entire space. A subunit descriptor reports a single measurement for each subunit in a scaffold and therefore represents a distribution over all subunits. An interunit descriptor reports measurements of elements that physically span the entire space and therefore also represents a distribution of data. Under each main heading, we have organized descriptors under relevant subheadings.

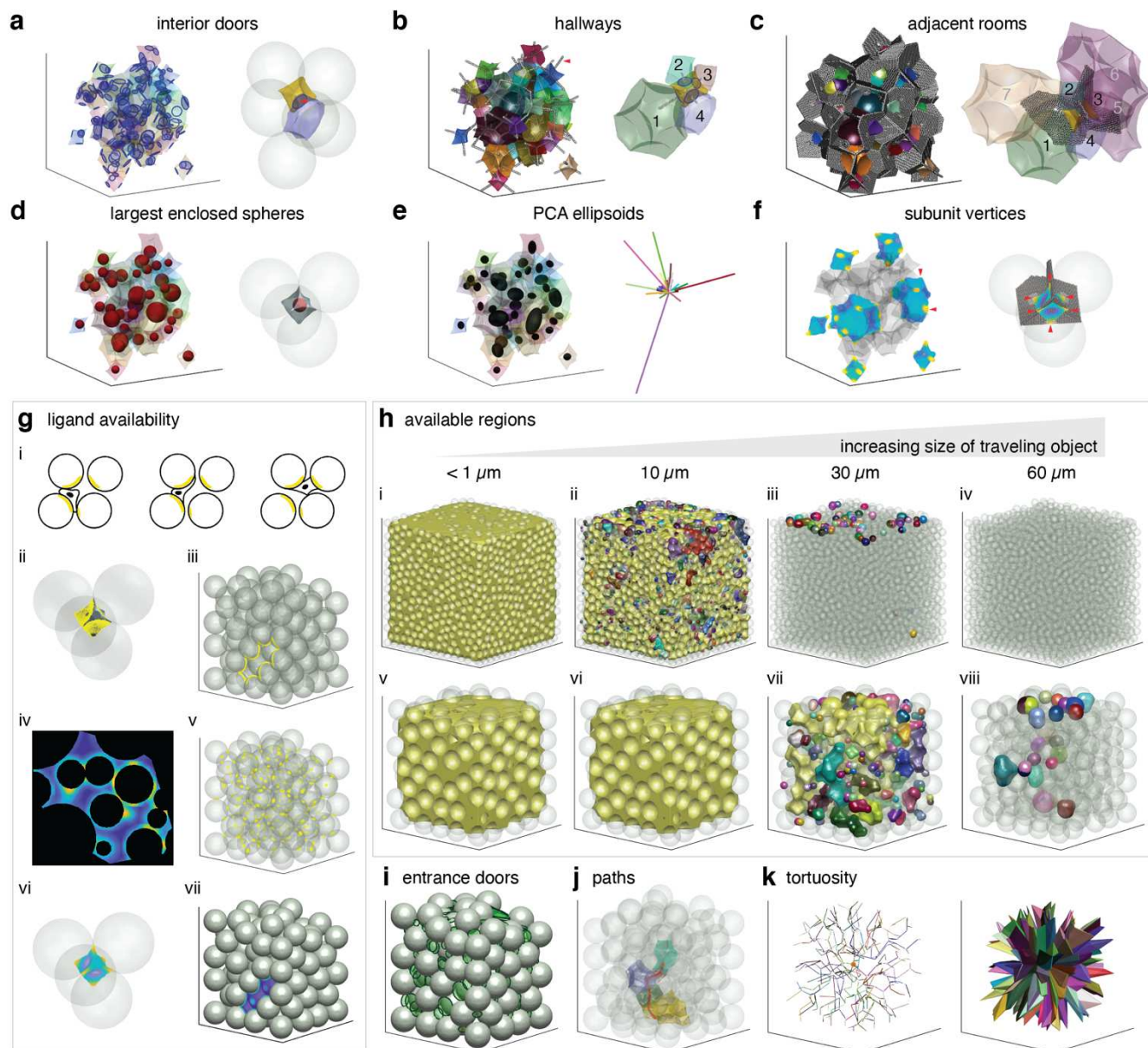


Figure 2 | LOVAMAP software computes scaffold descriptors that capture information about local void space geometry, ligand concentration, movement through scaffolds, and more. a, Doors of interior void space subunits, represented as blue circles. (Right) Individual door, indicated by red arrow, separating two ‘rooms’ (subunits). **b,** Hallways (1D-ridges) of interior subunits, which define neighboring subunits (single hallway indicated by red arrow). (Right) Hallways of a single subunit (yellow), showing neighboring rooms (1-4). **c,** 2D-ridges of interior subunits, which define adjacent subunits. (Right) Showing all adjacent rooms (1-7) of a single subunit (yellow). **d,** Largest enclosed spheres (red) of interior subunits, with a single subunit highlighted to the right. **e,** Ellipsoids (black) of interior subunits derived from principle component analysis (PCA). (Right) All major axes of the PCA ellipsoids shown on the left, scaled by their respective eigenvalues and translated to a common point. **f,** Subunit vertices or tips (yellow), indicated by red arrows. Showing seven select subunits only. (Right)

Showing the six 2D-ridges of a single subunit, which correlate to the number and location of the subunit's vertices (red arrows). **g**, Ligand availability. i, Cells within MAP scaffolds will adhere to surface ligands (yellow) and migrate across particle surfaces. ii, Accessible ligands for a single subunit correspond to the particle surfaces (yellow) that enclose the pocket of open space. iii, Accessible ligand along the perimeter of a single surface subunit (yellow). iv, Z-slice of ligand heatmap that represents the number of ligand molecules sensed by a migrating cell. v, Ligand hotspots (yellow) are regions of the ligand heatmap that contain greater than 2 million ligand molecules. vi, Ligand concentration (from ligand heatmap) of a single subunit. vii, Surface concentration (from ligand heatmap) of a single surface subunit. **h**, Accessible regions of void space highlighted with distinct colors. (i-iv) 40 μm diameter rigid microparticle scaffold. i, For objects less than 1 μm (e.g., molecules), the entire void space (yellow) is accessible. ii, For 10 μm objects (e.g., cells), objects are limited to distinct pockets of space, including the largest region (yellow). iii, For 30 μm objects (e.g., 3-cell cluster), a majority of the void space is inaccessible. iv, For 60 μm objects (e.g., 6-cell cluster), no objects can fit within the interior of the scaffold. (v-viii) 100 μm diameter rigid microparticle scaffold. v, The entire void space is accessible for < 1 μm objects, vi. The entire void space is accessible for 10 μm objects. vii, Distinct regions of space are accessible for 30 μm objects (largest region in yellow). viii, Distinct pockets of space are accessible for 60 μm objects. **i**, Exterior doors of scaffold, represented as green circles. **j**, Sample void space path highlighted in red; showing transparent void space subunits that are traversed by the path. **k**, (Left) Unique paths used to compute tortuosity-by-length (arc-to-chord ratio). (Right) Convex hull of unique paths used to compute tortuosity-by-volume. For corresponding descriptor images for square and hexagonal packing, see **Supplementary Figure 8**. For images of ligand heatmaps for atypical particle domains, see **Supplementary Figure 9**. For path images of domains containing mixtures of rigid and soft particles, see **Supplementary Figure 10**.

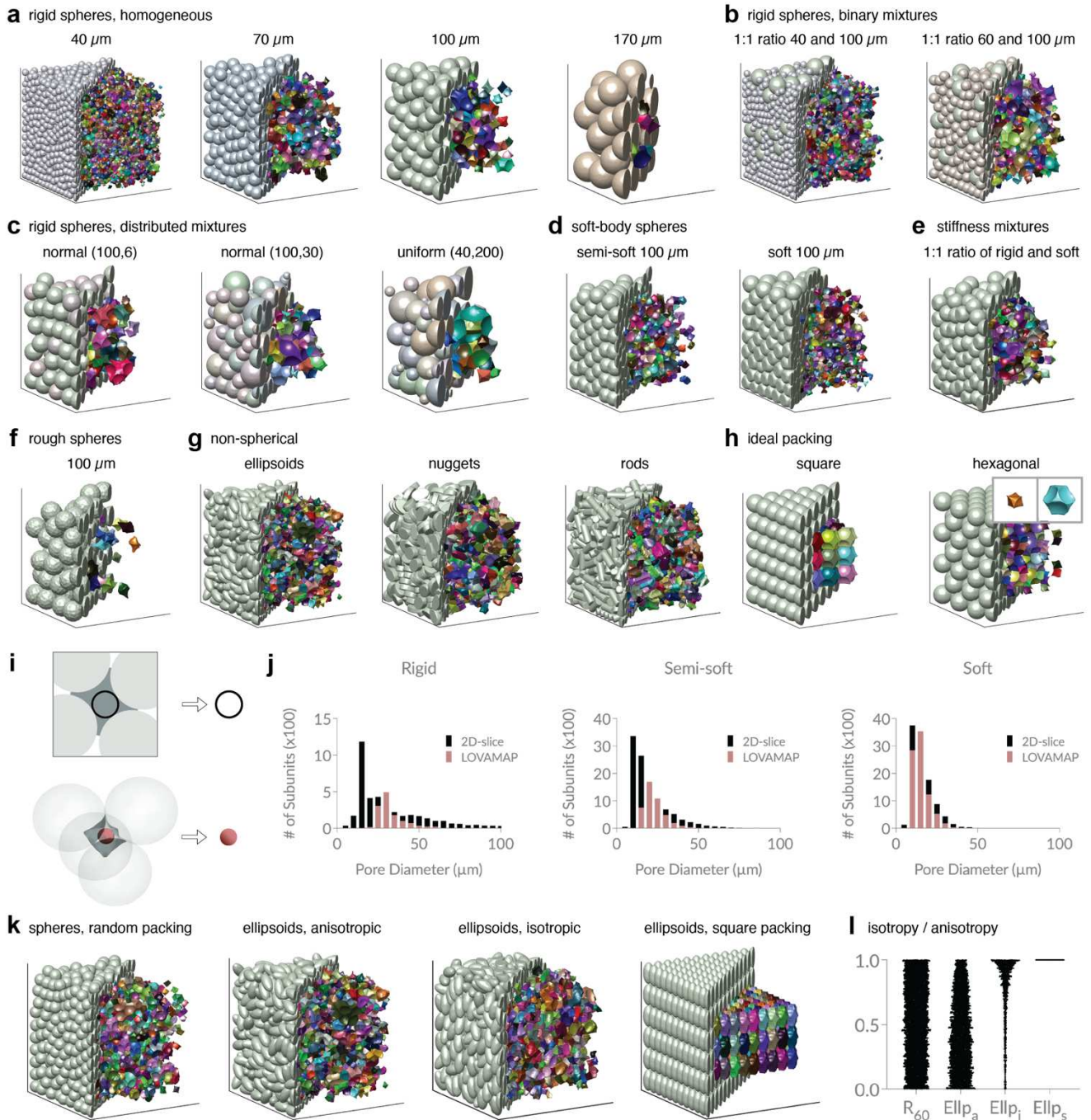


Figure 3 | Visual library of granular scaffold standards showing 3-D pores (subunits). a – h, Showcasing various particle domains and their corresponding interior subunits. For surface subunits, see **Supplementary Figure 11**. c, (left) Normal distribution with mean, μ , of 100 μm and standard deviation, σ , of 6 μm ; (middle) normal distribution with $\mu = 100 \mu\text{m}$ and $\sigma = 30 \mu\text{m}$; (right) uniform distribution with lower bound of 40 μm and upper bound of 200 μm . h, (right) Highlighting the two repeating subunits seen in hexagonal packing. i, Measuring ‘pore size’ using 2D-slices is compared against 3D-pores (subunits) generated by LOVAMAP. For 2D-slice analysis (top), an open region of void space (2D-subunit) is shown in dark grey, and the ‘pore size’ of the 2D-subunit is defined as the diameter of the largest enclosed circle (black outline). For 3D analysis, a subunit is shown in dark grey,

and the 'pore size' is measured as the diameter of the largest enclosed sphere (dusty rose). **j**, We compare pore size obtained using 2D-analysis vs. 3D-analysis for particle domains comprising 100 μm diameter spheres for three categories of particle stiffness: rigid, semi-soft, and soft ($n = 10$ each). For each scaffold, 2-D data refers to 2D-subunits from 30 evenly-spaced z-slices across the middle two-thirds of the scaffold, while 3-D data refers to all interior subunits. Results from the two-tailed Mann-Whitney test indicate that 2D-slice vs. LOVAMAP produces statistically different distributions for rigid and semi-soft domains ($p < 0.0001$), while the Kolmogorov-Smirnov test shows statistical difference for rigid, semi-soft, and soft domains ($p < 0.0001$). **k**, Showing particles and interior subunits of the following homogeneous domains: 60 μm diameter rigid spheres in random packing ($n = 10$); ellipsoids in random packing (anisotropic) ($n = 10$); ellipsoids in aligned orientation (isotropic) ($n = 1$); ellipsoids in perfect square packing ($n = 1$). **l**, Subunit isotropy / anisotropy descriptor outputs for the domain categories shown in (k), respectively. From left to right, data distributions shift from uniform (min = 0, max = 1) to non-uniform, indicating a shift from anisotropic to isotropic void space. These results support the notion that collective void space pore orientation follows collective particle orientation.

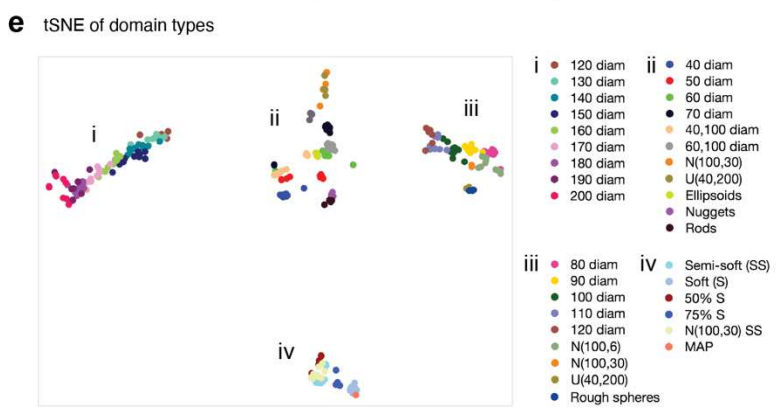
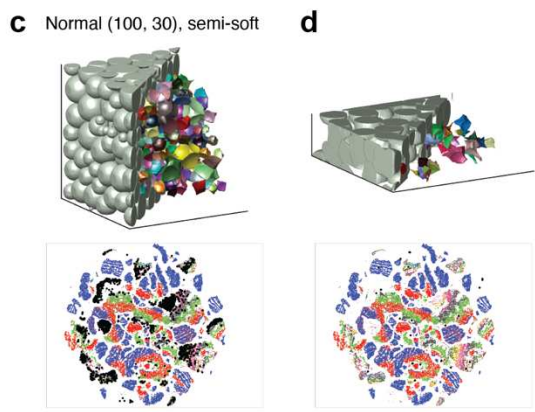
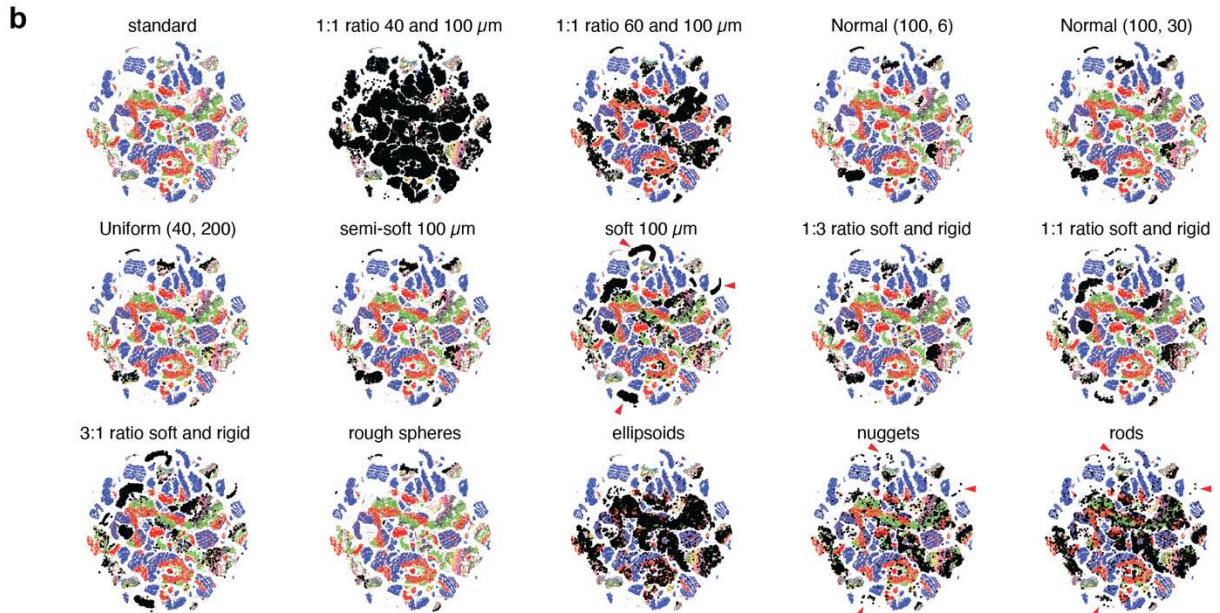
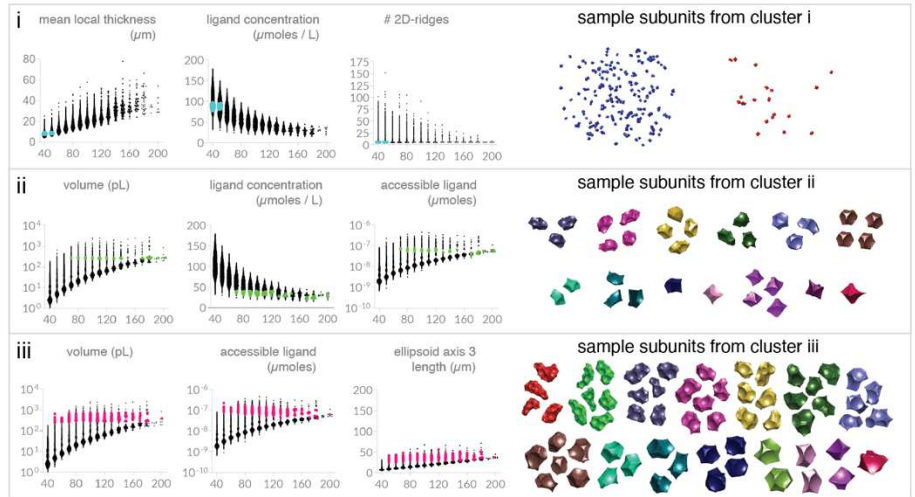
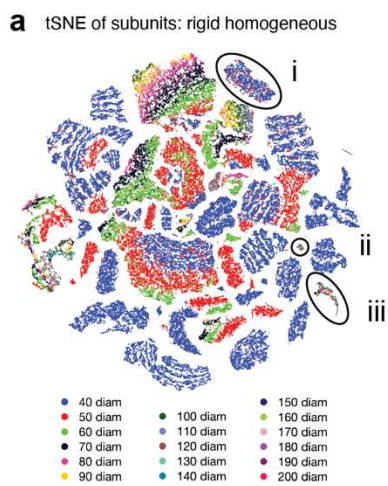


Figure 4 | T-distributed stochastic neighbor embedding (t-SNE) plots are used for higher-dimensional analysis of descriptor data. a, tSNE plot of subunits from homogeneous, rigid particle domains, where each datapoint represents an interior subunit that is identified by its 17 descriptor

values. Datapoints are colored according to their parent domain listed below. Three distinct clusters, i – iii, are highlighted for deeper analysis. For each cluster, we display three descriptors plots that exhibit similarity among the subunits and serve as key features that define the cluster. Subunits from cluster i, ii, and iii are overlaid in blue, green, and pink, respectively. To the right, we include sample subunits from each cluster, colored according to the tSNE plot key. For complete set of subunit data, see **Supplementary Data 30-32. b**, We overlay the cumulative subunits (in black) from each domain type onto the tSNE ‘standard’ plot of subunits from homogeneous, rigid particle domains. We observe similarities or differences between the void space of a given domain type relative to the homogeneous, rigid ‘standards’ by analyzing where subunits do or don’t cluster together. Red arrows in ‘soft 100 μm ’, ‘nuggets,’ and ‘rods’ highlight examples of clusters that are not found in domains comprising rigid, spherical particles. **c**, (top) We run LOVAMAP on a ‘realistic’ MAP scaffold simulated using semi-soft, spherical particles whose diameters follow a normal distribution (μ : 100, σ : 30). Image shows particles and interior subunits. (bottom) Resulting subunits are overlaid (in black) onto the tSNE ‘standard’ plot. **d**, (top) We run LOVAMAP on a real map scaffold of $\sim 100 \mu\text{m}$ diameter polyethylene glycol hydrogel microparticles that were imaged at 20x magnification using a Nikon C2 confocal microscope. Image shows particles and interior subunits. (bottom) Resulting subunits are overlaid (in black) onto the tSNE ‘standard’ plot. **e**, tSNE plot of particle domains, where each datapoint represents a particle domain that is identified by 247 descriptor-derived values. Datapoints are colored according to their parent domain. Domains contained within each distinct cluster (i – iv) are listed to the right. tSNE plots contain data from: 10 domains for rigid particle domains, homogeneous soft-body particle domains, and normal distribution of semi-soft particles; 5 domains for heterogeneous soft-body domains and atypical particle domains; 1 domain of a real MAP scaffold. Parameters for tSNE plots of subunits (perplexity: 15, learning rate: 500, exaggeration: 4) and tSNE plots of particle domains (perplexity: 20, learning rate: 500, exaggeration: 3). For tSNE plots of subunits from square and hexagonal packing, see **Supplementary Figure 12**.

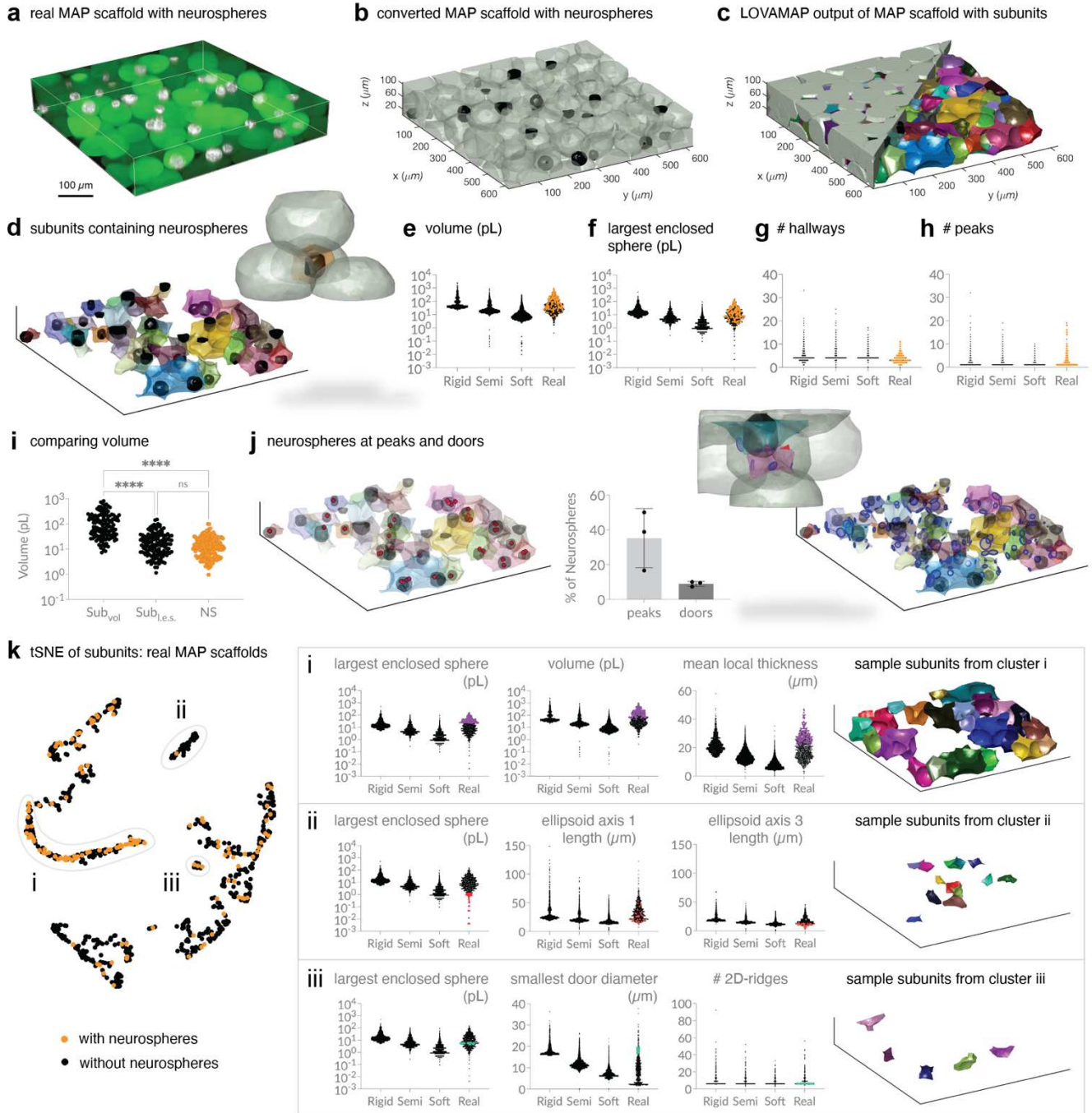


Figure 5 | LOVAMAP outputs are used to study neurosphere formation in MAP scaffolds. a, Confocal microscope image of MAP scaffold (green particles) with residing neurospheres (white) (Imaris software). **b,** MAP scaffold and neurospheres are converted to 'labeled' data using 3-D Particle Segmentation approach¹⁴. **c,** LOVAMAP segments scaffold void space into distinct 3-D pores (colored subunits). **d,** Highlighting void space subunits where neurospheres reside. (Right) Showcasing a sample subunit containing a single neurosphere surrounded by four particles that enclose the space. **e-h,** Comparing LOVAMAP subunit descriptor outputs of three simulated scaffolds (rigid, semi-soft, and soft 100 μm diameter particles; $n = 10$ domains each) against real MAP scaffolds ($n = 3$ replicate scaffolds; 2 regions of interest sampled in each). Subunits containing neurospheres are overlaid in

orange. **i**, For subunits containing neurospheres, we compare subunit volume (Sub_{vol}) and subunit largest enclosed sphere ($Sub_{l.e.s.}$) against residing neurosphere volume (NS). We find no significant difference between $Sub_{l.e.s.}$ and NS volumes (Kruskal-Wallis test, p-value 0.1109). **j**, Proportion of neurospheres at peaks compared to proportion at doors across three replicate scaffolds (p-value 0.0558). (Left) Showing which peaks (red) are within neurospheres. Many neurospheres are large enough to encompass multiple peaks. (Right) Showing all doors of visible subunits, for reference, but highlighting a neurosphere that resides at a door. This particular neurosphere also overlaps with a peak. **k**, tSNE plot of subunits from six MAP scaffold samples, where each subunit is identified by its 17 descriptor values. Subunits housing neurospheres are colored in orange. Cluster i contains proportionally many neurospheres, cluster ii contains only a single neurosphere, and cluster iii is a third distinct cluster that we chose to analyze. To the right, we show subunits from corresponding clusters that exist inside individual scaffolds. In favor of showing the relative position of subunits in their scaffolds, we did not adjust the viewing angle on an individual subunit basis, so it is not possible to fully appreciate the similarity in shape for all subunits shown. (perplexity: 20, learning rate: 500, exaggeration: 5).

Supplementary Files

This is a list of supplementary files associated with this preprint. Click to download.

- [RileyLSupplementaryMaterialsv2.pdf](#)